1 October 2002

Optics Communications 211 (2002) 53–63

OPTICS COMMUNICATIONS

www.elsevier.com/locate/optcom

# A 3D vectorial optical transfer function suitable for arbitrary pupil functions

Matthew R. Arnison *, Colin J.R. Sheppard

*Physical Optics Laboratory, School of Physics, University of Sydney, Sydney, NSW 2006, Australia*

Received 23 May 2002; accepted 27 June 2002

**Abstract**

We calculate the 3D vectorial optical transfer function directly from the vectorial pupil function, without making the paraxial assumption nor assuming radially symmetric pupils. Our model uses a single autocorrelation integral with Cartesian pupil co-ordinates to calculate the transfer function. Results for Herschel and aplanatic systems are presented. We discuss the meaning and application of a vectorial transfer function as a tool for analysing high aperture incoherent microscopy modes including fluorescence and transmission.


*PACS:* 42.30.Kq; 42.30.Lr; 07.60.Pb

*Keywords:* Optical transfer function; Fourier optics; Incoherent microscopy; Vectorial focusing; 3D image formation

## 1. Introduction

The transfer function is an important tool in optical design, where it is used to evaluate the performance of a given optical system. The optical transfer function (OTF) for a linear, space-invariant system is given by the Fourier transform of the intensity point spread function (PSF). Even if the system is not linear or space-invariant, the Fourier transform of the intensity PSF is a useful measure of the system performance, and is often termed the OTF. The 3D OTF describes the action of a lens in terms of spatial frequencies in the 3D PSF produced at the focus. By determining the system OTF, together with a model for the response of the object to incident light, we can build up a model for the system as a whole.

Maximising the performance of high resolution microscopy requires increasingly accurate models for the high numerical aperture lenses used, for the effects of their apodisation functions, and for any aberrations introduced by the the specimen. Vectorial theory for the accurate calculation of the high aperture PSF has been available for a long time [1–3]. Yet despite the popularity of Fourier optics for modelling low aperture systems, the field of high aperture vectorial transfer functions remains relatively unexplored.

* Corresponding author.
*E-mail addresses:* mra@physics.usyd.edu.au (M.R. Arnison), colin@physics.usyd.edu.au (C.J.R. Sheppard).
*URL:* http://www.physics.usyd.edu.au/physopt/.

0030-4018/02/$ - see front matter 
PII: S0030-4018(02)01857-6

Frieden [4] first derived the scalar 3D OTF as an autocorrelation using the paraxial approximation. This autocorrelation provides a method for calculating the OTF directly from the pupil function. This is much simpler than first obtaining the PSF and then performing a Fourier transform – especially in 3D. Frieden's work was extended by Sheppard et al. [5] to cover the scalar high numerical aperture ("high NA") case by explicitly avoiding the paraxial assumption. This work derived analytical expressions, assuming cylindrical symmetry in the pupil function. However, modelling arbitrary aberrations and pupil functions, and indeed using a vectorial approach taking account of the asymmetry of incident polarised light, requires a more general non-cylindrical model.

An alternative approach is to calculate the autocorrelation as a multiplication in Fourier space, allowing the use of the fast Fourier transfer (FFT) algorithm. This method was applied to vectorial pupil functions by Sheppard and Larkin [6], resulting in a vectorial OTF. This is a useful method, especially for 2D projections. However calculation using 3D FFTs would be awkward, delicate and time consuming due to the need for careful consideration of sampling issues, accuracy and the large 3D arrays required.

A vectorial OTF was also presented by Urbańczyk [7], but the analysis was restricted to a 2D OTF for low angle systems. The earliest mention of an incoherent scalar OTF with an axial dimension was by Mertz [8, pp. 101–102].

Our approach in this paper is to expand the development of two papers by Sheppard et al. [5,6], generalising where necessary to full 3D Cartesian co-ordinates, in order to avoid the assumption of radial symmetry. We present general descriptions of the vectorial lens pupil functions. This pupil function description is then used in an autocorrelation to form the vectorial OTF, which may be geometrically interpreted as the volume of overlap between two spherical shells.

We derive general formulas for the volume of overlap, which do not assume radial symmetry, resulting in a single integral. This equation is straightforward, if time consuming, to calculate, and serves as a useful alternative to the Fourier transform method [6]. We then plot the vectorial OTF for various cases. Finally we discuss the implications and potential uses of a vectorial OTF.

## 2. Vectorial pupil function

The theory of Richards and Wolf [3] describes how to determine the electric field near to the focus of a lens which is illuminated by a plane polarised quasi-monochromatic light wave. Their analysis assumes very large values of the Fresnel number, equivalent to the Debye approximation. We can then write the equation for the vectorial amplitude PSF $\vec{E}(\vec{x})$ of a high NA lens illuminated with a plane polarised wave as the Fourier transform of the complex vectorial pupil function $\vec{Q}(\vec{m})$ [9],

$$\vec{E}(\vec{x}) = -\frac{ik}{2\pi}\int\int\int \vec{Q}(\vec{m})\exp(ik\vec{m}\cdot\vec{x})\,d\vec{m}. \tag{1}$$

Here $k = 2\pi/\lambda$ is the wave number, $\lambda$ is the wavelength, $\vec{m} = (m,n,s)$ is the Cartesian pupil co-ordinate, and $\vec{x} = (x,y,z)$ is the focal co-ordinate. The vectorial pupil function describes the effect of a lens on the polarisation of the incident field, the complex value of any amplitude or phase filters across the aperture, and any additional aberration in the lens focusing behaviour from that which produces a perfect spherical wavefront converging on the focal point.

Because we are describing the behaviour of electromagnetic waves, they must obey the Maxwell equations, giving an important constraint – the homogeneous Helmholtz equation for time-independent vectorial wave fields,

$$\nabla^2\vec{E}(\vec{x}) + k^2\vec{E}(\vec{x}) = 0, \tag{2}$$

assuming a constant refractive index in the focal region.

By expressing the Helmholtz equation in Fourier space, we can determine the electromagnetic constraints on the pupil function $\vec{Q}(\vec{m})$. Applying the Fourier relationship $\nabla^2\vec{E}(\vec{x}) \Longleftrightarrow -|\vec{m}|^2\vec{Q}(\vec{m})$, we have

$$(|\vec{m}|^2 - k^2)\vec{Q}(\vec{m}) = 0, \tag{3}$$

which means that the pupil function is only non-zero on the surface of a sphere with radius $k$,

$$\vec{Q}(\vec{m}) = \vec{P}(\vec{m})\delta(|\vec{m}| - k^2). \tag{4}$$

This is known as the Ewald sphere in the theory of X-ray diffraction.

For a practical quasi-monochromatic wave, $k$ cannot have purely a single value, so the spread of wavelengths in the illumination light gives a small finite thickness to the spherical shell. For this paper we examine the monochromatic case and assume a thin shell of thickness $\delta k$ and take the limit $\delta k \to 0$.

Because the pupil function only exists on the surface of a sphere, we can slice it along the $s = 0$ plane into a pair of functions

$$\vec{Q}(\vec{m}) = \vec{Q}(\vec{m})\frac{k}{s}\delta\left(s - \sqrt{k^2 - l^2}\right) + \vec{Q}(\vec{m})\frac{k}{s}\delta\left(s + \sqrt{k^2 - l^2}\right), \tag{5}$$

representing forward and backward propagation. Here we have introduced a radial co-ordinate $l = \sqrt{m^2 + n^2}$. The $k/s$ factor accounts for the change in projected thickness of the spherical shell for declination angles away from the $s$ axis, a side-effect of rewriting the delta function in terms of $s$ rather than the radius $|\vec{m}|$.

Now we examine the axial projections $\vec{P}_{\pm}(m,n)$ of the pupil function,

$$\vec{P}_{+}(m,n) = \int_0^{\infty} \vec{Q}(\vec{m})\,\mathrm{d}s, \tag{6}$$

$$\vec{P}_{-}(m,n) = \int_{-\infty}^{0} \vec{Q}(\vec{m})\,\mathrm{d}s, \tag{7}$$

which represent forward and backward propagation, respectively. Together these 2D functions give a complete description of the 3D pupil function $\vec{Q}(\vec{m})$. Restricting our attention to the forward propagation case, we can write

$$\vec{P}_{+}(m,n) = \int_0^{\infty} \vec{Q}(\vec{m})\frac{k}{s}\delta\left(s - \sqrt{k^2 - l^2}\right)\mathrm{d}s \tag{8}$$

$$= \vec{Q}(m,n,s_{+})\frac{1}{s_{+}}, \tag{9}$$

where we have normalised the radius to $k = 1$ and indicated the constraint on $s$ to the surface of the sphere with $s_{+} = \sqrt{1 - l^2}$.

The aperture of the lens is represented by slicing a cap off the top of the sphere. The angle $\alpha$ subtended by the cap at the centre of the sphere is related to the numerical aperture NA and the refractive index $n$ of the imaging medium (such as air, water or immersion oil) by

$$\sin\alpha = \frac{\mathrm{NA}}{n} \tag{10}$$

as shown in Fig. 1.

For incident light which is plane-polarised along the $x$ axis, we can derive a vectorial strength function $\vec{a}(m,n)$, from the strength factors used in the vectorial PSF integrals [3,6,10]

$$\vec{a}(m,n) = \begin{pmatrix} (m^2 s_{+} + n^2)/l^2 \\ -mn(1 - s_{+})/l^2 \\ -m \end{pmatrix}, \tag{11}$$

where we have converted from the spherical polar representation in Richards and Wolf to Cartesian co-ordinates. We show an example case for $\vec{a}(m,n)$ in Fig. 2.

We can now model polarisation, apodisation and aperture filtering as amplitude and phase functions over the projected pupil,

$$\vec{P}_{+}(m,n) = \frac{1}{s_{+}}\vec{a}(m,n)S(m,n)T(m,n) \tag{12}$$

representing forward propagation only ($\alpha \leqslant \pi/2$), where $S(m,n)$ is the apodisation function, and $T(m,n)$ is any complex transmission filter applied across the aperture of the lens. This transmission

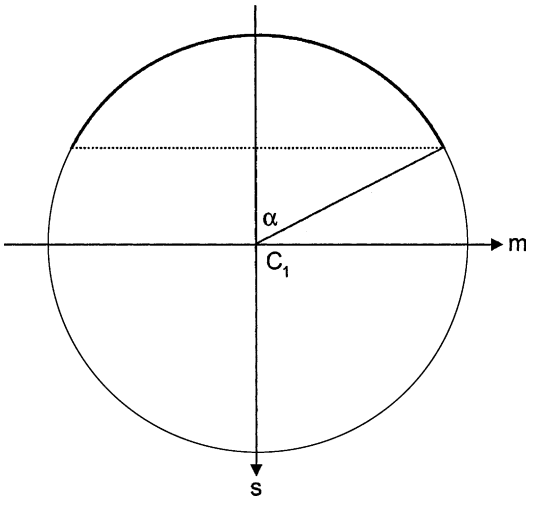


Fig. 1. A cross-section through the pupil sphere in the $(m,s)$ plane.

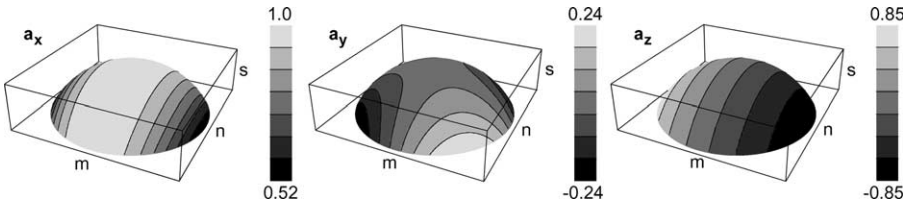


Fig. 2. The vectorial strength factors $\vec{a}(m,n)$ for linearly polarised light propagating in the forward direction, mapped onto the spherical pupil caps, with $\alpha = \pi/3$.

factor can also be used to model focusing aberrations.

For uniform focusing, the Herschel condition, the apodisation function is simply

$$S_{\mathrm{h}}(m,n) = 1. \tag{13}$$

Microscope objectives are usually designed to obey the sine condition, giving aplanatic imaging [11], for which we write the apodisation as

$$S_{\mathrm{s}}(m,n) = \cos^{1/2}\theta \tag{14}$$

$$= \sqrt{s_+}. \tag{15}$$

## 3. Three-dimensional vectorial optical transfer function

For incoherent imaging, we are interested in using the OTF to describe the frequency components of the intensity $\vec{E}\cdot\vec{E}^*$ of the PSF. From (1) and the Fourier autocorrelation theorem [12],

$$|f(\vec{x})|^2 \Longleftrightarrow \int\int\int F\left(\vec{m}+\frac{\vec{m}'}{2}\right)F^*\left(\vec{m}-\frac{\vec{m}'}{2}\right)\mathrm{d}\vec{m} \tag{16}$$

(where $\vec{F}(\vec{m})$ is the Fourier transform of $\vec{f}(\vec{x})$), we can obtain the OTF $\vec{C}(\vec{K})$ by taking the autocorrelation of the pupil function $\vec{Q}$,

$$C(\vec{K}) = \int\int\int \vec{Q}\left(\vec{m}+\tfrac{1}{2}\vec{K}\right)\cdot\vec{Q}^*\left(\vec{m}-\tfrac{1}{2}\vec{K}\right)\mathrm{d}\vec{m}. \tag{17}$$

The spatial frequency $\vec{K} = (m,n,s)$ may be represented geometrically as the shift of one copy of the pupil sphere cap relative to the other. The total value of the integral for a given spatial frequency $\vec{K}$ is given by the total volume of intersection of the shifted spherical shells, multiplied at each intersection point by the values of the pupil functions at that location.

The spheres intersect in a circle perpendicular to the direction of the shift between them, which we call the *circle of intersection*, as shown schematically in Fig. 3. When the spheres are shifted so far that they no longer intersect, the value of the OTF for that shift must be zero, giving the absolute spatial frequency cutoff.

At any given point along the circle of intersection, the intersection between the spherical shells

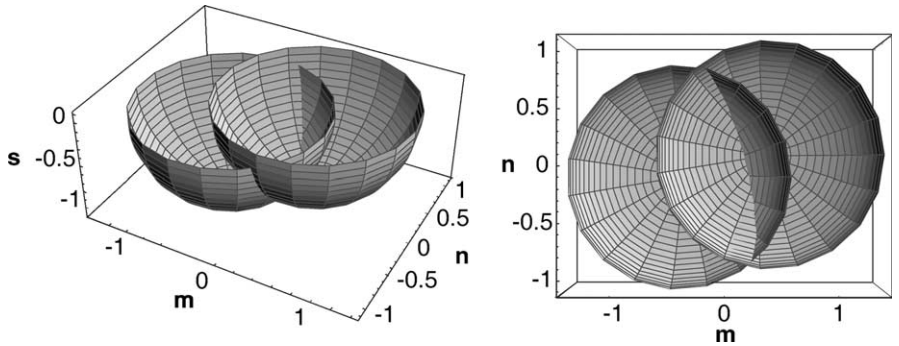


Fig. 3. 3D views of the shifted spherical pupil caps for $K = (0.8, 0.2, 0.2)$ and $\alpha = \pi/2$. The intersection can be seen as the arc of a circle.

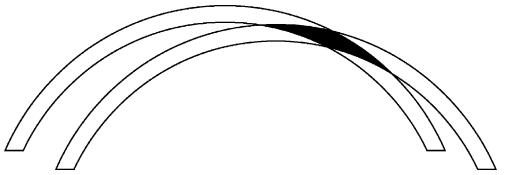

Fig. 4. The rhombic area of overlap between two spherical pupil caps.

has a rhombic cross-section (Fig. 4). Therefore for any pupil shift $\vec{K}$ we need to find a general equation for the circle of intersection, so that we can find the value of the shifted pupil functions along the circle, and also an equation for the area of the rhombic cross-section.

For convenience we denote the total length of the pupil shift as $K$

$$K = |\vec{K}| = \sqrt{m^2 + n^2 + s^2}. \tag{18}$$

Cross-sections of the geometry for the intersecting spheres are shown in Figs. 5 and 6. The shifted pupil spheres can be described using vectors as

$$|\vec{m} \pm \vec{K}/2| = 1 \tag{19}$$

allowing us to solve for the radius of the circle of intersection of the two spheres

$$r_0 = |\vec{r}_0| = \sqrt{1 - \frac{K^2}{4}}. \tag{20}$$

If we can fully specify the circle of intersection using a vector equation for one case, we can use vector scaling and rotation to produce the circle of intersection for any given $\vec{K}$. Setting $\vec{K}_0 = (K, 0, 0)$, the circle of intersection for this case is

$$\vec{r}_0(\vec{K}_0, \beta) = \begin{pmatrix} 0 \\ r_0 \sin\beta \\ -r_0 \cos\beta \end{pmatrix}, \tag{21}$$

where $\beta$ is introduced as a parameter to isolate a point on the circle by its angle with the $s$ axis.

We now generalise for arbitrary $\vec{K}$. Changes in the length of $\vec{K}$ are accommodated already by Eq. (21). Rotation of $\vec{K}$ whilst keeping $\beta = 0$ at the lowest $s$ co-ordinate on the circle can be described using a pair of counter-clockwise Euler rotations,

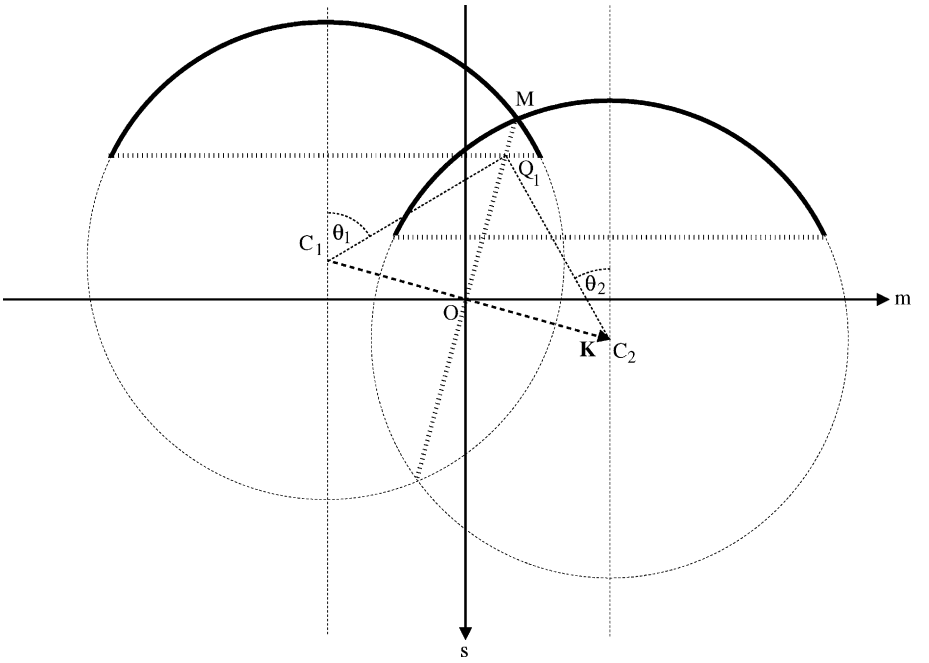


Fig. 5. A cross-section through the intersecting spheres for a given offset between them of $\vec{K}$. For the purposes of this figure, we assume $n = 0$. The radius $r_0$ of the arc of intersection is shown here as OM. $Q_1$ is the projection of $P_1$ from Fig. 6, the endpoint of the arc of intersection where $\beta = \beta_1$.

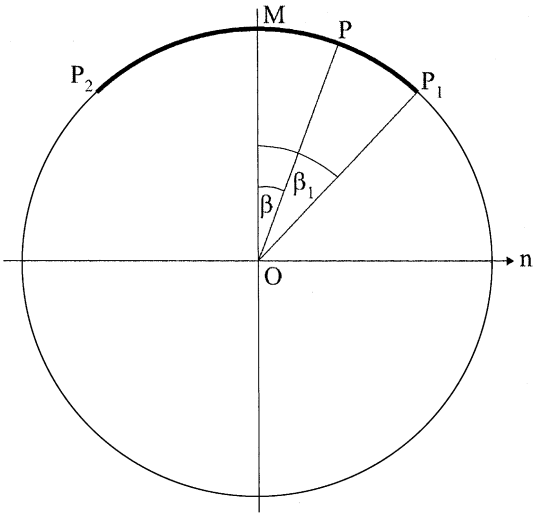


Fig. 6. The circle of intersection, in the plane along the line MO that is perpendicular to the $(m,s)$ plane of Fig. 5 (again assuming $n=0$ for the purposes of the figure). The arc of intersection is shown as $P_1MP_2$, which varies with spatial frequency $\vec{K}$ and aperture angle $\alpha$. For a constant pupil, the length of this arc, $2\beta_1(\vec{K},\alpha)$, is proportional to the strength of the transfer function for a given spatial frequency $\vec{K}$.

$$\vec{R}_n(\theta)=\begin{pmatrix}\cos\theta & 0 & -\sin\theta\\ 0 & 1 & 0\\ \sin\theta & 0 & \cos\theta\end{pmatrix}, \tag{22}$$

$$\vec{R}_s(\phi)=\begin{pmatrix}\cos\phi & \sin\phi & 0\\ -\sin\phi & \cos\phi & 0\\ 0 & 0 & 1\end{pmatrix} \tag{23}$$

first about the $n$ axis, then around the $s$ axis, giving a general form for the circle of intersection,

$$\vec{r}_0(\vec{K},\beta)=\vec{R}_s[-\arctan(n/m)]\times\vec{R}_n[\pi/2-\arccos(s/K)]\vec{r}_0(\vec{K}_0,\beta) \tag{24}$$

$$=\begin{pmatrix} r_0\frac{1}{lK}[ms\cos\beta-nK\sin\beta]\\ r_0\frac{1}{lK}[ns\cos\beta+mK\sin\beta]\\ -r_0\frac{l}{K}\cos\beta\end{pmatrix}, \tag{25}$$

where $\arctan(n/m)$ takes account of which quadrant $(m,n)$ is in.

Finally, we need to incorporate the rhombic shape of each intersection area along the circle of intersection (Fig. 4). By geometry, this shape will be constant around any given circle, but will vary according to the shift $\vec{K}$ between the pupils. The area $A$ of the rhombus is given by

$$A(\vec{K})=\frac{(\delta k)^2}{Kr_0} \tag{26}$$

for $K>0$, giving a line integral. For $K=0$ the integral becomes a surface integral proportional to $\delta k$. For infinitely thin shells, the line and surface integrals cannot be numerically compared. Since we are obviously more interested in the range $K>0$, we focus on the line integral in this paper, for which $C(\vec{0})\to\infty$. This represents the average value of the PSF intensity, which diverges due to the spatially unbounded behaviour of the PSF in Eq. (1).

Having accounted for the changing cross-section, we can now recast the autocorrelation using the projected vectorial pupil function $\vec{P}_+(\vec{m})$ from Eq. (12), and integrate along an arc of the circle of intersection, giving an unnormalised equation for the autocorrelation

$$C_{\mathrm{UnNorm}}(\vec{K})=\frac{(\delta k)^2}{K}\int_{-\beta_1}^{\beta_1}\vec{P}_+[\vec{r}_0(\vec{K},\beta)+\tfrac{1}{2}\vec{K}]\cdot\vec{P}_+^{*}[\vec{r}_0(\vec{K},\beta)-\tfrac{1}{2}\vec{K}]\,\mathrm{d}\beta, \tag{27}$$

where $\beta_1$ is the highest possible angle $\beta$ on the circle of intersection for a given aperture $\alpha$, shown as $\mathrm{MOP}_1$ in Fig. 6, and defined below in Eq. (33). This allows us to integrate along the complete arc of intersection between the spheres.

Two-dimensional (2D) and one-dimensional (1D) OTFs are usually normalised against the zero frequency value. However, for the 3D case, Eq. (27) gives a singularity at $C(\vec{0})$. Instead we choose to normalise against the total volume of the OTF. By the Fourier definite integral theorem, this is equivalent to the central value of the intensity PSF, which we easily determine [3]. We use uniform (Herschel) apodisation for determining the normalisation. Setting $|\vec{E}(\vec{0})|^2=1$, the normalisation factor is

$$N(\alpha)=\left\{\frac{1}{4}(3+\cos^2\alpha)\sin^4\frac{\alpha}{2}\right\}^2. \tag{28}$$

We now arrive at a normalised form of the 3D vectorial OTF that is easy, albeit time consuming, to calculate

$$C(\vec{K}) = \frac{1}{KN(\alpha)} \int_{-\beta_1}^{\beta_1} \vec{P}_+[\vec{r}_0(\vec{K},\beta) + \tfrac{1}{2}\vec{K}] \cdot \vec{P}_+^*[\vec{r}_0(\vec{K},\beta) - \tfrac{1}{2}\vec{K}]\,\mathrm{d}\beta. \quad (29)$$

Note that we have made no assumptions about the symmetry of the pupil function $\vec{P}$ nor any assumptions of low aperture, and therefore this equation is suitable for calculating the 3D vectorial OTF with arbitrary pupil functions and apertures. However, there remains some symmetry in $C(\vec{K})$ by virtue of the fact that we defined it as the Fourier transform of a real function, the intensity PSF. This constraint results in Hermitian symmetry in the OTF,

$$C(\vec{K}) = C^*(-\vec{K}). \quad (30)$$

It is helpful to note that the angles $\theta_{1,2}$ at the centres of the spheres between the $s$ axis and the point of intersection, as shown in Fig. 5, are given by

$$\cos\theta_{1,2}(\vec{K},\beta) = -\vec{r}_0(\vec{K},\beta)\cdot\hat{\vec{s}} \mp \frac{s}{2} = r_0\frac{l}{K}\cos\beta \mp \frac{s}{2}. \quad (31)$$

We now need to find the appropriate limits on the integration to ensure we only calculate in physical zones, avoiding regions where the spherical caps do not intersect. These conditions define the spatial frequency cutoff:

1. If the *spheres* are shifted by more than twice their radius, then they will never intersect. Therefore
$$K \leqslant 2. \quad (32)$$
2. The aperture will set a limit $|\beta| \leqslant \beta_1$ on the *length of the arc* of the circle of intersection. This limit can be found by geometry, substituting $\theta_1 = \alpha$ into Eq. (31) and solving for $\beta$
$$\beta_1(\vec{K},\alpha) = \begin{cases} \arccos\left\{\frac{K}{lr_0}\left(\frac{|s|}{2}+\cos\alpha\right)\right\}, \\ \quad \text{if } \frac{K}{lr_0}\left|\frac{|s|}{2}+\cos\alpha\right| \leqslant 1 \\ 0, \text{ if } \mathrm{Re}\left\{\frac{K}{lr_0}\left(\frac{|s|}{2}+\cos\alpha\right)\right\} > 1 \\ \pi, \text{ if } \mathrm{Re}\left\{\frac{K}{lr_0}\left(\frac{|s|}{2}+\cos\alpha\right)\right\} < -1. \end{cases} \quad (33)$$
The inequality conditions cover cases where the full spheres intersect, but the aperture $\alpha$ truncates the caps before that point, or for regions where for large apertures $\alpha > \pi/2$ the arc of intersection completes a full circle.
3. It is useful for certain calculations to know the spatial frequency cutoff in terms of limits on $\vec{K}$, which may be determined using [5]
$$2(l\sin\alpha - |s|\cos\alpha) = K^2. \quad (34)$$

## 4. Results

We evaluated Eq. (29) for Herschel and sine apodisations at a very high aperture ($\alpha = 2\pi/5 \Rightarrow \mathrm{NA} = 0.95$ in air) to explore the OTF behaviour under conditions unsuitable for modelling with low NA techniques. Calculations were performed using standard Mathematica integration routines, on a Linux system with an AMD Athlon 1.4 GHz processor. Large plots such as the one in Fig. 8 took about 4 h, while Fig. 9 took 20 min. A major speed boost could be expected if the integration was coded in C instead of using Mathematica.

Evaluating the vectorial OTF gives substantial numerical territory to explore. Each 3D point within the spatial frequency cutoff has a scalar

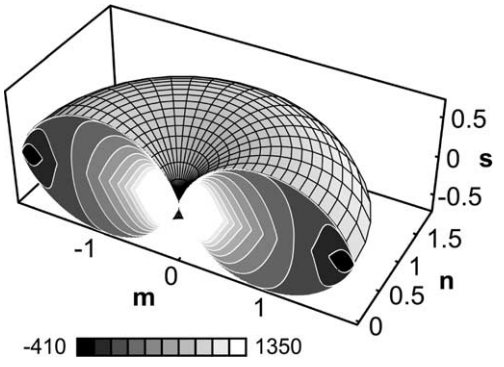


Fig. 7. A schematic of the 3D vectorial OTF for $\alpha = 2\pi/5$ with Herschel apodisation. The mesh surface indicates the spatial frequency cutoff, outside which the OTF is zero. This surface has been sliced at $n = 0$, revealing the amplitude $C(m,0,s)$ on that plane of the 3D OTF, after taking the sum of all vector components.

value which may be split up into 3 contributions from the vectorial components of the pupil,

$$C = Q_x \bigstar Q_x^* + Q_y \bigstar Q_y^* + Q_z \bigstar Q_z^* \tag{35}$$

$$= C_x + C_y + C_z. \tag{36}$$

The symbol ★ denotes autocorrelation. A general overview of the shape of the OTF is given in Fig. 7, showing the surface of the cutoff and the total value of the OTF for a slice through the function.

Fig. 8 shows transverse slices through the vectorial OTF for $s = 0$, with sine apodisation. $C_x$ shows changing asymmetry across the $m$ and $n$ axes. At lower frequencies, the OTF along the $m$ axis is stronger than along the $n$ axis, while at high frequencies the situation is reversed. $C_y$ has a dramatic fourfold symmetry and large negative

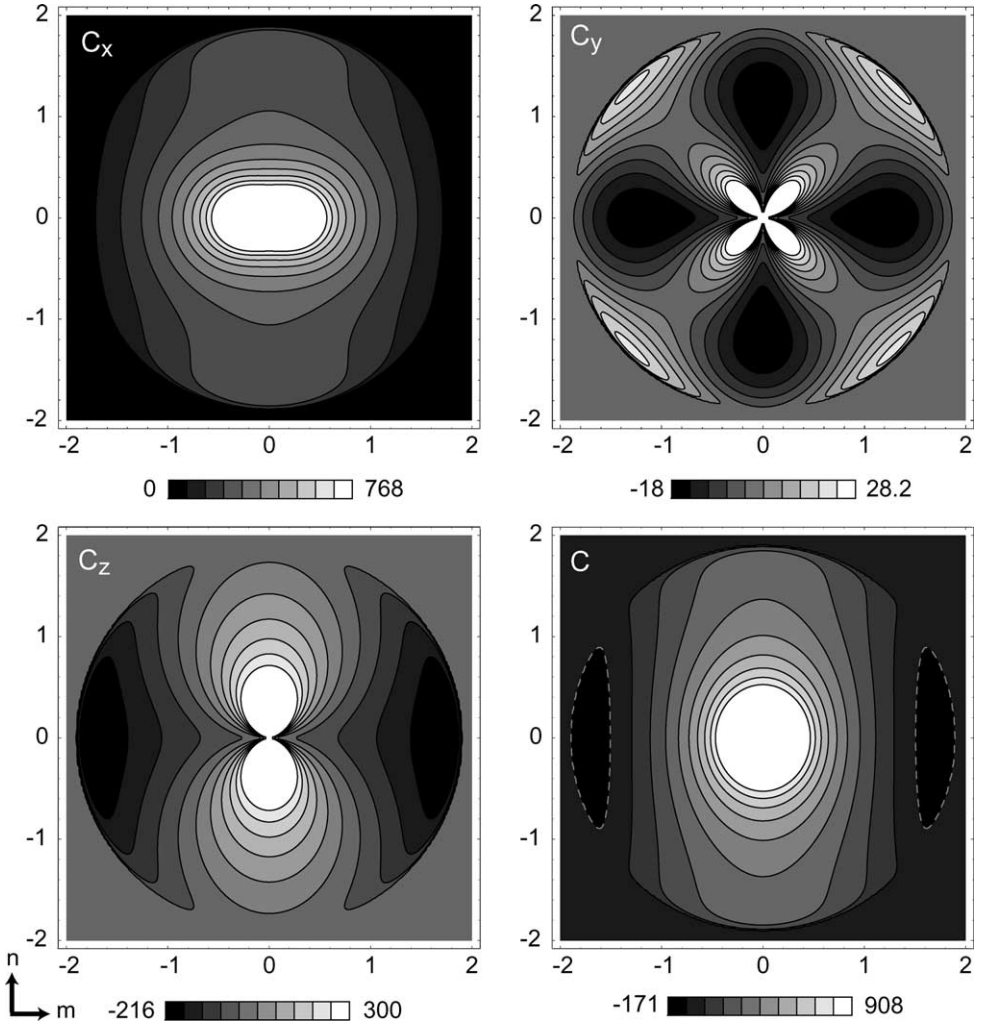


Fig. 8. Transverse slices through the vectorial OTF for $s = 0$, with $\alpha = 2\pi/5$ and sine apodisation. The vector components and total amplitude are shown as $C_x$, $C_y$, $C_z$, and $C$. Each plot is independently scaled, due to the large differences in amplitude for the different components. Note that in this paper we have assumed input linear polarisation along the $x$ axis, corresponding to the $m$ axis in frequency space. $C_x$ shows an interesting asymmetry, with a low $x$ frequency boost (central horizontal elongation), yet a high $y$ frequency (vertical elongation) boost. The total amplitude $C$ includes negative regions (indicated with a dashed contour line) at high values of $m$, inherited from $C_z$.

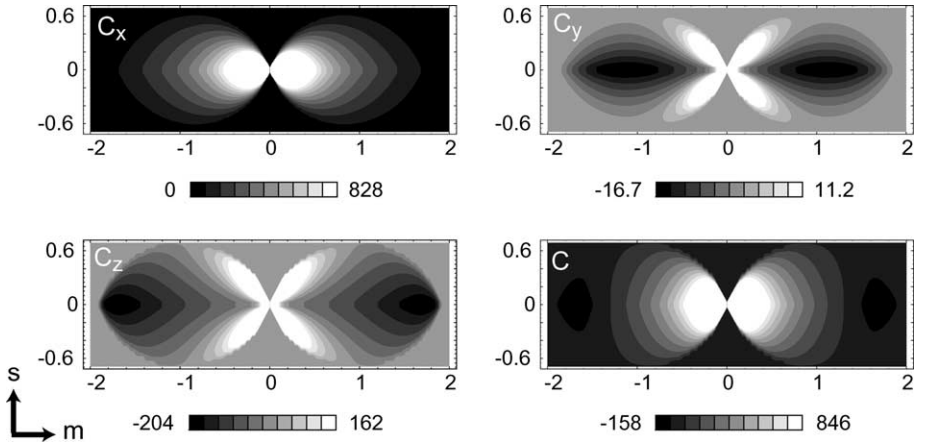


Fig. 9. Axial slices through the vectorial OTF for $n = 0$, with $\alpha = 2\pi/5$ and sine apodisation. The vector components and total amplitude are shown. As for the transverse slices, the $C_y$ component in particular shows interesting structure. However $C_y$ is very weak compared with the other components, so this will not have a very large effect overall.

regions, but this component of the OTF is orthogonal with the input polarisation and has relatively little strength. However, $C_z$ has substantial energy including negative regions with about 30% of the peak strength of $C_x$. This results in a total OTF $C$ with large negative regions which indicates a contrast reversal for high frequencies parallel to the $x$ axis in the PSF. While the general characteristics are similar to Figs. 7–10 of Sheppard and Larkin [6], we emphasise that Fig. 8 is of *slices* through the OTF rather than the projections shown in Sheppard and Larkin.

Fig. 9 shows axial slices through the vectorial OTF for $n = 0$, with sine apodisation. For this case the most dramatic features away from the $s = 0$ plane are to be seen in the $C_y$ component. However, again, this component contributes relatively little to the total OTF.

To enable more direct comparison with Sheppard and Larkin [6] we have plotted in Fig. 10 the total amplitude $C' = C'_x + C'_y$ of the *projection* through $s$ of the OTF

$$C'(m,n) = \int C(m,n,s)\,\mathrm{d}s \tag{37}$$

with sine apodisation. By the projection–slice theorem [13], this corresponds to the spatial frequencies in a transverse slice along the focal plane of the PSF. With a negative region of about 10% of the value of the low frequency response, significant contrast reversal can be expected for high $m$ transverse frequencies, while the $n$ frequencies are stronger overall than the $m$ frequencies as has been noted before [3,11] in direct studies of the vectorial PSF.

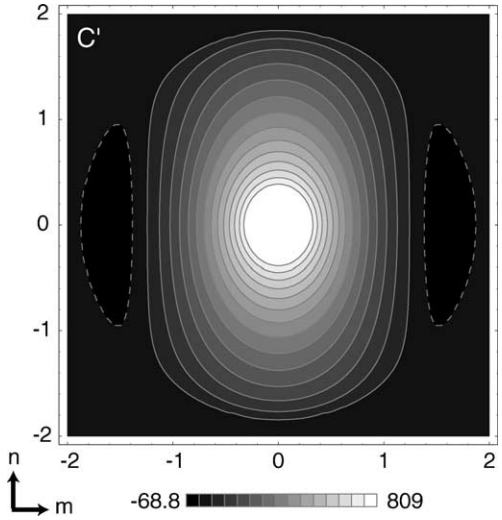


Fig. 10. The amplitude $C'$ of the projection through $s$ of the vectorial OTF for $\alpha = 2\pi/5$ and sine apodisation. This is equivalent to figure 10 of Sheppard and Larkin [6] except for the change to sine apodisation. The dashed contour lines at the extreme left and right of the figure enclose the negative regions of $C'$.

Calculating the projected OTF in this manner is very time-consuming, taking about 12 h on our Linux Athlon system. The 2D FFT approach described by Sheppard and Larkin [6] is thus much more efficient for calculation of projections.

## 5. Discussion

The vectorial OTF is a relatively new concept in optical imaging theory, and raises substantial questions of interpretation and meaning. Clearly there are significant asymmetries introduced at high NA for polarised light. However, their application to modelling an entire imaging system is less straightforward than for standard 2D transfer functions as used in Fourier optics.

The vectorial OTF presented here is simply a representation of the frequency content of the intensity pattern in the focal region of a single lens illuminated by a linearly polarised plane wave. It could be argued, therefore, that the term vectorial OTF is not appropriate, and that it should be called instead the vectorial intensity spatial frequency spectrum. However, we have chosen to use the shorthand notation of vectorial OTF, as the OTF is well known to represent the spatial frequency content of the intensity PSF in scalar 2D optics.

The performance of a system will depend on the imaging behaviour of at least one lens, and the vectorial response of the specimen. For example, to apply this theory to fluorescence microscopy, we need to use a model of the dipole orientation, rotation and response of the excited molecules for varying incident polarisation and spatial frequency [14]. By incorporating this dipole response model, the vectorial OTF might form an important tool in modelling the frequency response of entire imaging systems. If the dipole can freely rotate, then the image in a confocal fluorescence microscope is the same as for an isotropic point object [15] and we can use the appropriate vectorial OTF directly.

For modelling incoherent transmission microscopy of weakly scattering objects, we can assume a linear system. Again, knowledge of the response of the object to different polarisations and spatial frequencies of light is required for producing a vectorial OTF representing the system as a whole. In this way, the 3D vectorial OTF might be useful for analysing polarisation microscopy.

For strongly scattering objects or changes in specimen refractive index, a more complicated approach is needed [16].

Our use of the Debye approximation assumes a high Fresnel number. However, unless the Fresnel number is infinite, regions of the PSF very far from focus will have smaller Fresnel numbers. Since each point in the OTF naturally encompasses Fourier components from throughout the theoretically infinite extent of the PSF, the Debye approximation places a limit on the accuracy of the OTF. While in general the contributions of regions away from focus will be small due to the concentration of power at focus, this approximation will be a concern for very strong aberrations which distribute significant energy away from the focal point.

Typically aberrations in paraxial systems are modeled using Zernike polynomials describing the phase variation across a circular pupil [17], and this is a useful tool in Fourier optics. Some aberrations, such as defocus or spherical aberration can be described using the radial pupil co-ordinate alone, but, in general, aberrations depend on both the radial and polar co-ordinate. Although Zernike polynomials are not orthogonal for high aperture systems, due to their assumption of a flat 2D pupil, clearly any general description of aberrations will allow for radial asymmetry. This provides a further justification for OTF calculation methods which make no assumptions of symmetry.

A high NA equivalent of the Zernike functions is needed, defined on the cap of a sphere rather than across a circle, to describe focusing aberrations [18]. In addition, the relationship between the causes of aberrations, such as a refractive index change in the specimen, needs to be carefully mapped from rigorous PSF models onto the pupil function [19,20].

Modelling amplitude and phase masks placed in the back focal plane of the lens is somewhat simpler – they can be applied directly to the model presented here using the complex transmission filter $T(m,n)$.

In conclusion, we have presented an autocorrelation based method for evaluating the high NA

vectorial OTF using a simple line integral. Arbitrary pupil functions may be used without the need for cylindrical symmetry. We have plotted slices and a projection through the vectorial OTF for unaberrated focusing with sine and Herschel apodisation. Although in principle the same information is contained in the PSF, the OTF makes it easier to see frequency-based focusing characteristics.

For OTF projections, FFT-based methods are more efficient as long as care is taken with accuracy and sampling effects. In addition, such projections of the OTF only carry information about a single plane of the PSF, and care must be used when including them as part of a system model.

In general, our autocorrelation method for calculating the vectorial OTF has the advantage of being straightforward to evaluate for arbitrary pupil functions and arbitrary points in the OTF.

## Acknowledgements

We thank Peter Török for illuminating discussions about the meaning of high aperture optical transfer functions. We also thank both Peter Török and Carol Cogswell for their helpful comments on the manuscript. This work was supported by the Australian Research Council.

## References

[1] V.S. Ignatowsky, Trans. Opt. Inst. Petrograd 1 paper 4 (1919) 1.
[2] V.S. Ignatowsky, Trans. Opt. Inst. Petrograd 1 paper 3 (1920) 1.
[3] B. Richards, E. Wolf, Proc. R. Soc. A 253 (1959) 358.
[4] B.R. Frieden, J. Opt. Soc. Am. 57 (1967) 56.
[5] C.J.R. Sheppard, M. Gu, Y. Kawata, S. Kawata, J. Opt. Soc. Am. A 11 (1994) 593.
[6] C.J.R. Sheppard, K.G. Larkin, Optik 107 (2) (1997) 79.
[7] W. Urbańczyk, Opt. Acta 33 (1) (1986) 53.
[8] L. Mertz, Wiley, New York, 1965.
[9] C.W. McCutchen, J. Opt. Soc. Am. 54 (1964) 240.
[10] M. Mansuripur, J. Opt. Soc. Am. A 3 (12) (1986) 2086.
[11] H.H. Hopkins, Proc. Phys. Soc. 55 (1943) 116.
[12] R.N. Bracewell, second ed., McGraw-Hill, New York, 1978.
[13] R.N. Bracewell, Prentice-Hall, Englewood Cliffs, NJ, USA, 1995.
[14] P. Török, C.J.R. Sheppard, in: A. Diaspro (Ed.), Confocal and Two-photon Microscopy: Foundations, Applications and Advances, Wiley-Liss, New York, 2002, p. 127.
[15] C.J.R. Sheppard, P. Török, Bioimaging 5 (1997) 205.
[16] A. Rohrbach, E.H.K. Stelzer, J. Opt. Soc. Am. A 18 (4) (2001) 839.
[17] M. Born, E. Wolf, Principles of Optics, seventh ed., Cambridge University Press, Cambridge, UK, 1999.
[18] C. Sheppard, Optik 105 (1) (1997) 29.
[19] P. Török, P. Varga, Z. Laczik, G.R. Booker, J. Opt. Soc. Am. A 12 (2) (1995) 325.
[20] P. Török, Opt. Mem. Neural Netw. 8 (1) (1999) 9.